

Plasmascopy of ultrafast hot charges in solids

Dmitry A. Zimin,¹ Raja Sen,² Muhammad Qasim,³ Jelena Sjakste,⁴ Vladislav S. Yakovlev^{3,5}

¹Laboratory of Physical Chemistry, Department of Chemistry and Applied Biosciences, ETH Zürich, Vladimir-Prelog-Weg 2, 8049, Zürich, Switzerland.

²SATIE, CNRS, ENS Paris-Saclay, Université Paris-Saclay, Gif-sur-Yvette, 91190, France.

³Max-Planck-Institut für Quantenoptik, Hans-Kopfermann-Straße 1, 85748 Garching, Germany.

⁴Laboratoire des Solides Irradiés, CEA/DRF/IRAMIS, École Polytechnique, CNRS, Institut Polytechnique de Paris, 91120 Palaiseau, France.

⁵Fakultät für Physik, Ludwig-Maximilians-Universität, Am Coulombwall 1, 85748 Garching, Germany.

Abstract

We demonstrate an electric field-resolved approach for probing ultrafast dynamics of photoinjected charges in solids. Direct access to the electric field of few-cycle pulses enables us to measure a broadband response of a medium with associated plasma frequency. We prepare an ensemble of photoinjected hot charge carriers with energies sufficient to trigger impact ionization and establish a framework to measure its dynamics. Our study reveals the first time-resolved observation of the short-lived ultrafast impact ionization in germanium counteracted by trapping of mobile charges at later times. This approach provides a promising route for studying ultrafast many-body physics in photoexcited solids, with predictions from advanced theoretical models.

Teaser

Time- and electric field-resolved measurements reveal ultrafast plasma frequency dynamics in a semiconductor.

Introduction

Detailed understanding of hot carrier dynamics in semiconductors is crucial for advancing the performance of optoelectronic devices and enabling new functionalities, where the ability to manipulate and control hot charges becomes increasingly important (1). The main challenge here is that carrier relaxation involves a complex interplay of interactions among electrons, holes, and phonons (2). Impact ionization is one of important consequences of this interplay with a central role in charge transport, energy dissipation, and device operation. For instance, carrier multiplication increases the light-conversion efficiency beyond the Shockley–Queisser limit. In semiconductor p–n junctions, it triggers the avalanche breakdown. In photodetectors, it is harnessed to achieve internal gain required for fiber-optic communications and low-light detection. These advantages however can be negated by opposing mechanisms that reduce the number of mobile charges.

Ultrafast photoinjection of charge carriers triggers a complex sequence of processes, each characterized by distinct timescales and dominant physical mechanisms. For highly photoexcited charges (typically, with excess energies exceeding the second conduction band minimum), the fastest processes are the loss of interband coherence and momentum scattering due to electron-electron coupling. This typically happens on a $\lesssim 10$ femtoseconds (fs) (2–4) timescale, which is too short for substantial energy transfer from carriers to the lattice. Consequently, by the end of this stage, electrons and holes get redistributed in the reciprocal space (5), while their energy distributions are largely preserved, which is known as momentum equilibration (6, 7). Simultaneously electrons and holes may undergo impact ionization if the excess energy of photoexcited charges is higher than the material band gap. The carriers can also get trapped as well as undergo trap-assisted or Auger recombination (13). The timescales of these competing processes depend on the defect density, carrier density and excess energy of carriers, leading to a transient nature of the overall effect. For instance, an increase of the charge density may be present only for a short time until it is overshadowed by a slower trapping mechanisms.

These ultrafast transient dynamics are difficult to access experimentally. The time- and angle-resolved photoemission spectroscopy (tr-ARPES) provides the most direct information about occupations of Bloch states (2). The measurements however must be performed under ultra-high vacuum conditions; the short mean free path of the photoemitted electrons makes the technique surface-limited; the trade-off between the temporal and momentum resolutions, imposed by the uncertainty principle, puts a limit on the fastest accessible processes. The transient absorption (14, 15) or reflection spectroscopy (10, 16, 17) provide only indirect limited access since the valuable information imprinted on the temporal profile of light is lost.

Electric field-resolved time-domain spectroscopy, offers a direct access to the electric field of light and preserves the full information. These measurements are standard to the terahertz (THz) domain but challenging at petahertz-scale frequencies. The picosecond-scale duration of THz pulses however is not sufficient to capture ultrafast femtosecond dynamics, while a narrow bandwidth limits the accuracy of the extraction of the complex frequency dependent material polarization. Recent advances have extended the measurement bandwidth up to petahertz frequencies (18–24) and single photon sensitivity (25), thus enabling electric field-resolved studies with extreme sensitivity, sub-fs temporal resolution (26) and a broad bandwidth.

In this work we present an electric field-resolved approach for accessing ultrafast scattering dynamics of photoexcited hot charges in solids. Our approach preserves the full response, but in contrast to THz studies, the response is imprinted on broadband few-cycle optical pulses. This allows us obtaining a broadband dynamic complex permittivity and associated plasma frequency (ω_{pl}) with unprecedented temporal resolution. Since the plasma frequency

$$\omega_{\text{pl}} = 2\pi \sqrt{\frac{e^2 N}{\epsilon_0 m_{\text{eff}}}} \quad (1)$$

is governed by the charge density and the effective mass, we use it as an observable to probe ultrafast charge density dynamics in a photoexcited solid. Here e is an elementary charge, ϵ_0 is the vacuum permittivity, N is photoexcited charge density and m_{eff} is the reduced effective mass of carriers averaged over all the occupied states, which is also known as the optical effective mass (15, 27).

Since in our study we aim for the ultrafast many-body hot carrier dynamics, we focus on germanium, due to its low bandgap that is favorable for the impact ionization. We observe a transient evolution of the plasma frequency that indicates two competing mechanisms which we relate to the first time-resolved observation of the ultrafast impact ionization in germanium opposed by a charge trapping dynamics.

Results

We realize a broadband field-resolved pump-probe study of hot charges with energies sufficient for impact ionization in germanium. For this we employ a recently developed GHOST (23) technique to measure, the electric field of a test pulse after transmission through a polycrystalline 290-nm film of germanium (Fig. 1A).

The carrier-envelope phase (CEP) stable injection pulse with a duration of 2.7 fs (full width at half maximum of intensity) was used to photoexcite the medium and to confine the photoexcitation event to a temporal window shorter than expected hot-carrier relaxation time. The octave-spanning spectrum (1.24 – 2.48 eV) is well above the indirect (0.67 eV) and direct (0.8 eV) band gaps of germanium. Some carriers injected by this pulse have sufficient energy to create new electron-hole pairs via impact ionization (the lowest photon energy required for this is $2 \times 0.67 = 1.34$ eV). We varied the peak electric-field strength of the injection pulse between 0.08 V/Å and 0.15 V/Å (in the focal plane, with no sample).

To record the non-equilibrium changes in the medium permittivity, we use a weak CEP-stable, 21-fs test pulse with a central wavelength of 2.1 μm . Prior to photoinjection, germanium is transparent to the test spectrum (0.4 - 0.65 eV). The field strength was kept low to ensure the linearity of the polarization response. We record the transmitted test electric field for various injection-test delays and various peak field strengths of the injection pulse. To illustrate how photoinjection reshapes the test electric field, we show three such waveforms in Fig. 1B, but a typical measurement consisted of 70 delays and 3 measurements per delay.

From the measured photoexcitation-induced changes in the test electric field, we calculate the change in the complex permittivity (Fig. 2). The emergence of electron-hole plasma decreases the real part of the permittivity, while the positive values of $\text{Im}[\Delta\epsilon]$ mean that the photoexcited sample absorbs light at frequencies where the band gap prohibits single-photon transitions in the unperturbed sample. Once all the electron-hole pairs recombine, the medium must return to its original state: $\Delta\epsilon(\omega) \equiv 0$. From Fig. 2, we see that, for the largest pump-probe delay in our measurements, this process is still far from completion. The local maxima of $\text{Im}[\Delta\epsilon]$ at 0.47 eV and 0.56 eV indicate resonant interband transitions. According to our *ab initio* calculations (see Methods), these are likely to be transitions between valence-band Bloch states around Γ point. These resonances are clearly visible even at $\tau=499$ fs with no notable change in their positions.

We now focus on the electron-hole plasma created by the injection pulse and associated plasma frequency, ω_{pl} . We retrieve ω_{pl} by fitting the measured $\Delta\epsilon(\omega)$ to a model that accounts for both the electron-hole plasma response and resonant interband transitions. We find that the Lindhard-Lorentz model

$$\Delta\epsilon(\omega) = -\frac{\omega_{pl}^2}{(\omega + i\gamma_{pl})^2} - \sum_l \frac{a_l}{\omega_l^2 - 2i\gamma_l - \omega^2}. \quad (2)$$

provides better agreement with our experiment than Drude-Lorentz approximation (Figs. 2b and 2c). Here, γ_{pl} represents the relaxation rate and determines the strength of electron-hole plasma absorption. The sum on the right-hand side consists of Lorentz terms, each describing resonant absorption at a frequency ω_l with a damping rate γ_l , where a_l controls the strength of the resonance. The key distinction between the Lindhard-Lorentz and Drude-Lorentz models lies in the first term: in the Drude model, it is $-\omega_{pl}^2/(\omega^2 + i\gamma_{pl}\omega)$. The Lindhard approximation has a more rigorous quantum-mechanical foundation as it accounts for the collective behavior of electrons in the random-phase approximation (28).

Before we analyze the plasma frequency retrieved from our data, let us illustrate our theoretical predictions for state occupations immediately after the interaction with the injection pulse. In Figs. 3A and 3B, we show the band structure of germanium and the density of states calculated with the Elk code (29) using the Tran-Blaha modified Becke-Johnson exchange-correlation pseudopotential (30). In Fig. 3C, we show the Brillouin-zone averaged probability to find a carrier in a state with a certain energy, which we calculated by solving the time-dependent Schrödinger equation in the basis of Kohn-Sham orbitals as described in (31). The same averaging over crystal momenta corresponds to what is believed to be the first stage of relaxation after photoinjection: long before the electrons and holes thermalize, electron-electron, electron-impurity, and short-wavelength (intervalley) electron-phonon scattering redistribute them in reciprocal space such that the occupation of any Bloch state depends only on the state's energy and not on its crystal momentum, which we refer to as momentum equilibration (11, 12). For our experimental conditions, we estimate that if electron-phonon interaction were the only contributing process, momentum equilibration would take 11–33 fs for electrons and 8–9 fs for holes (see Methods). The energy exchange between electrons and phonons is negligible during such a short time interval—we estimate the corresponding rate of energy transfer to be in the order of 1–2 eV/picosecond (see Methods). Consequently, the energy distribution is expected to change negligibly during momentum equilibration. Fig. 3C shows that the injection pulse indeed occupies states where the carrier energy is sufficient for impact ionization. Although these occupations are small, the high density of states at these energies makes impact ionization a significant effect. Fig. 3C also illustrates that, at the highest intensities used in our measurements, photoinjection cannot be described as single-photon absorption (17), in which case occupations would depend linearly on the laser intensity, and the shapes of two curves in this figure would be nearly identical.

With these considerations in mind, we can analyze the dependence of the measured plasma frequency (Eq. 1) on the peak electric field of the injection pulse E_0 and the time after photoinjection t . The full circles in Fig. 4A summarize the measurement results. Although m_{eff} increases with increasing E_0 (31, 32), the plasma frequency takes larger values for stronger injection pulses because the increase in m_{eff} is offset by the increase in the concentration of electron-hole pairs, N . What is more intriguing is the dependence of ω_{pl} on time. The steady decrease of the plasma frequency for $t \gtrsim 100$ fs may look like an expected outcome of relaxation, but the electron-hole recombination is supposed to be negligible within the interval of pump-probe delays that we consider here (13, 33). Furthermore, as carriers lose their energies (e.g., by generating phonons)

and gather at the bottoms of the L, Γ , and X valleys, where band curvature is largest, their optical effective mass must decrease (15), which would be expected to increase the plasma frequency. In the measurements, however, an increase in the plasma frequency can be observed only during the first few tens of fs after photoinjection, after which ω_{pl} decreases with time. A possible explanation for this steady decrease could be intervalley scattering from the bottom of the Γ valley, where the effective electron mass is $m^* = 0.05 m_e$, to the bottom of the L valley, where the effective DOS mass is $m^* = 0.2 m_e$ (34), which can cause the optical effective mass to increase. However, the scattering time of this process is 230 fs (35), whereas the plasma frequency decrease we see in Fig. 4A is a much slower process. If the main contribution here comes not from the time dependence of the optical effective mass but from a decrease in carrier concentration, N , then we have to consider two possibilities: Auger recombination and carrier trapping. The rate of Auger recombination is known to be proportional to N^3 (for intrinsic semiconductors), which allows us to rule it out as a dominant process. Indeed, when E_0 changes from 0.05 V/Å to 0.15 V/Å, the concentration of carriers must increase by roughly a factor of 3, thus increasing the rate of Auger recombination by more than an order of magnitude, while Fig. 4A shows no significant speed up in the relaxation of the plasma frequency for stronger injection pulses. Thus, the only plausible explanation for these observations is that, during the first 500 fs after photoinjection, a significant number of carriers ends up trapped in defect states, which should be abundant in the polycrystalline germanium. This conclusion is consistent with transient-absorption measurements (13).

We attribute the initial increase in ω_{pl} during the first few tens of fs to the impact ionization. Photoinjected electrons with sufficient energy can excite valence electrons to the conduction band through inelastic collisions shortly after photoinjection, which increases N and thus also increases ω_{pl} . Since impact ionization causes a redistribution of charge carriers in momentum space, it also results in a corresponding change in the optical effective mass. Studies of impact ionization dynamics (36, 37) confirm that most such collision events must occur on the same time scale where we observe the transient increase in the plasma frequency (~ 100 fs). To support the above considerations, we demonstrate that the measured $\omega_{\text{pl}}(t, E_0)$ can be approximated by a model that captures three key physical processes: impact ionization, carrier trapping, and the field-strength-dependent effective mass m_{eff} . We used the following model:

$$\omega_{\text{pl}}(t, E_0) = a \sqrt{\frac{E_0^2}{E_0^2 + E_1^2} \left(e^{-\gamma_1 t} - \frac{b e^{-\gamma_2 t}}{E_0^2 + E_2^2} \right)}. \quad (3)$$

The first term under the square root describes the slow decrease in the plasma frequency at large times, while the second term describes its increase shortly after photoinjection. The corresponding rates are $\gamma_1 = 5.6 \times 10^{-4} \text{ fs}^{-1}$ and $\gamma_2 = 0.02 \text{ fs}^{-1}$, respectively, and they are independent of time and E_0 . The model captures the linear dependence of ω_{pl} on E_0 in the weak-field regime, as well as deviations from the $\omega_{\text{pl}}^2 \propto N \propto E_0^2$ scaling due to initial-state depletion, charge screening (38), and the dependence of the optical effective mass on E_0 . We account for these effects through intensity-dependent denominators in Eq. (3), which limit the increase in the plasma frequency at high intensities. The solid curves in Fig. 4A show the fit results with the following parameters: $a = 3.8 \text{ fs}^{-1}$, $b = 0.013$, $E_1 = 0.23 \text{ V/Å}$, and $E_2 = 0.049 \text{ V/Å}$. While physically motivated, this six-parameter model primarily serves to fit our data and extract the characteristic time scales: $\gamma_1^{-1} = 1.8 \text{ ps}$ for carrier trapping, which is consistent with (13), and $\gamma_2^{-1} = 50 \text{ fs}$ for the initial increase in plasma frequency.

While Fig. 4a emphasizes the dependence of ω_{pl} on time, Fig. 4b shows the dependence of ω_{pl} on the injection field strength for 32 fs and 499 fs times. This again indicates that the relaxation

dynamics of hot charges differ significantly on timescales below and above 50 fs confirming two competing mechanisms. Our fit model that considers two competing processes with $\gamma_2^{-1} = 50$ fs and $\gamma_1^{-1} = 1.8$ is consistent with our experiment.

Discussion

In our experiments, we observed that, after photoinjection by a few-fs laser pulse, the plasma frequency first increases during the first ~ 100 fs and then decreases on the picosecond time scale. We note that due to square root dependence of the plasma frequency, the 100 fs dynamics corresponds to 50 fs charge dynamics. We argue that the dominant contribution to the initial increase in ω_{pl} must come from impact ionization, which increases the carrier concentration and decreases the effective mass. The subsequent decrease in ω_{pl} at a rate too fast for electron-hole recombination implies a decrease in carrier concentration, which we attribute to carrier trapping. To verify this, we perform *ab initio* calculation of the energy-dependent photoexcited charge density (see Methods) and apply theoretical energy-dependent impact ionization rates derived from a Monte Carlo model (37). We integrate over all energies to obtain the temporal evolution of the total charge density, incorporating charge trapping phenomenologically (see Methods). Using Eq. (1), we estimate the time-dependent plasma frequency. Fig. 4c shows the result of our model together with the measured temporal changes in the plasma frequency at three highest injection field strength. Our estimation is based on the dynamic of the charge density only although the plasma frequency (Eq. 1) also depends on the effective mass. However, since the impact ionization redistributes charges in the momentum space, we expect impact ionization-induced change of the effective mass to be synchronized with the dynamic of the charge density. We find a good quantitative agreement of our impact ionization model with the experiment considering the trapping time constant of 1.27 ps. Fig. 4c highlights the importance of charge trapping in polycrystalline germanium. This explains why the impact ionization effect is entirely suppressed by charge trapping after about 50 fs.

We have demonstrated a new approach for investigating ultrafast hot charges in solids: pump-probe plasmascopy. The broadband nature of our experiment allows us to accurately extract the plasma frequency in spite of broad absorption peaks. Due to the square root dependence of ω_{pl} on the charge density and the effective mass we effectively trace these quantities that are encoded in a slower observable — the plasma frequency — thereby relaxing experimental demands for accessing ultrafast processes. When the test pulse duration is sufficiently short compared to the timescale of changes in medium properties, the polarization response can be represented by the frequency-dependent, complex-valued permittivity—an approach we adopted in this work. However, a general formalism exists for describing the response of dispersive media with time-dependent properties (26).

We established a fit formula that together with our experiment suggest two competing mechanisms which we attribute to the impact ionization and trapping of photoinjected charges. To further validate our findings, we conceived an *ab initio* based impact ionization model and found a good agreement with the experiment revealing the first time-resolved measurement of the impact ionization in germanium. Finally, we find that this effect is short-lived as it is quickly overshadowed by charge trapping.

This approach is quite general and can be applied to other materials and phenomena under various conditions providing a promising route for testing ultrafast, many-body physics in photoexcited solids with predictions from advanced theoretical models. For instance, Auger recombination or momentum equilibration (6, 7) in conventional materials, or correlated effects in quantum materials.

Materials and Methods

Experimental Design

The experiments were performed with a beamline that delivers CEP-stable 2.7-fs optical pulses centered at about 750 nm wavelength (26). Pulses from a Ti:Sapphire oscillator (Femtolasers) were amplified in a chirped-pulse amplifier at a repetition rate of 3 kHz, delivering pulses of 21 fs duration with 2.5 W average power. The pulses were spectrally broadened in a hollow-core fiber and further compressed in a multi-pass chirped mirror compressor (Ultrafast Innovations) to about 2.7 fs (19) duration (full width at half-maximum of intensity). The pulses were characterized in previous experiments using attosecond streaking (39) and non-linear photoconductive sampling (19). The pulses were split into three optical arms (more detail in (26)), named as sampling, test, and injection. The test arm was down-converted in spectrum via intrapulse difference-frequency generation (iDFG) in a type II BiB₃O₆ (BiBo) crystal. The generated pulses centered at about 130 THz were further compressed with a combination of thin silicon and fused silica plates providing 12 fs (full width at half-maximum of intensity) duration. Silicon plates were also used to block the fundamental spectrum after the iDFG process. The pulses were further recombined using broadband metallic wire-grid polarizers, while pulse energy in each arm was set by additional thin wire grid polarizers in each arm. The transmitted test pulse waveform was measured with a GHOST metrology (23) using ~12-μm-thick z-cut α-quartz crystal. The measurement of reference and modified (due to the excitation arm) waveforms was conducted with semi-simultaneous detection scheme (26) for high sensitivity.

Simulations of ultrafast photoinjection

We modeled the interaction of a 3.5-fs, 800-nm pump pulse with a germanium crystal by numerically solving the time-dependent Schrödinger equation (TDSE) in the basis of Kohn-Sham states obtained from density functional theory (DFT). We used the Tran-Blaha modified Becke-Johnson exchange-correlation pseudopotential (30) in the Elk code (29). The DFT calculations provided energies and momentum-operator matrix elements for 14 bands below the Fermi energy and 41 conduction bands on a 32×32×16 Monkhorst-Pack k-grid, yielding a direct band gap of 0.84 eV. Using this data, we solved the TDSE in the velocity gauge as described in (40). To generate Fig. 3C, we modeled momentum equilibration (7) neglecting inelastic scattering. Under the assumption that carriers maintain their energies during redistribution in reciprocal space, we calculated the equilibrated probabilities $p(\epsilon)$ for electron occupation of a Bloch state at energy ϵ using conservation of carrier number and energy. For this calculation, we used the following equation as a starting point:

$$\int_{-\infty}^{\epsilon} d\epsilon' p(\epsilon') \text{DOS}(\epsilon') = \frac{2}{N_k} \sum_{\epsilon_n(\mathbf{k}) \leq \epsilon} f_n(\mathbf{k}), \quad (4)$$

where DOS is the density of states, N_k is the total number of k-grid nodes, $f_n(\mathbf{k})$ is the occupation of the Bloch state in band n at crystal momentum \mathbf{k} , and the factor 2 accounts for spin degeneracy due to the absence of spin-orbit interaction in our DFT calculations. This approach allowed us to perform averaging without introducing energy bins, which would be problematic because, even with $N_k = 16384$, only a few Bloch states will be found in a few-meV energy interval. Instead, we evaluated the right-hand side of Eq. (4) and then used the Savitzky-Golay filter with third-order polynomials to evaluate the derivative with respect to ϵ , which resulted in $p(\epsilon) \text{DOS}(\epsilon)$. With the known density of states, we then calculated $p(\epsilon)$ and plotted it in Fig. 3C.

We also performed *ab initio* calculations of $\Delta\epsilon(\omega)$ using the model from (31). In these simulations, we observed absorption peaks similar to the ones in Fig. 2. These resonances formed at 0.48 eV, 0.60 eV, and 0.63 eV, showing a small deviation from the measured resonances at 0.47 eV and 0.56 eV. This discrepancy likely originates from the neglected spin-orbit interaction. For the 0.48-eV resonance, we identified its origin as the excitation of holes from the light-hole band to the next lower-energy band at $k = 0.052$ atomic units (the reciprocal lattice vectors have a length of 1.02 atomic units).

To calculate the electron-phonon scattering times, germanium was described within density functional theory and density functional perturbation theory (DFPT) using Quantum ESPRESSO (41), Wannier90 (42) and EPW (43) codes. Computational details for Ge can be found in (2).

Impact ionization model

After obtaining the energy dependent occupations of electrons [$p_e(\epsilon)$] and holes [$p_h(\epsilon)$] followed by the photoinjection, we evaluate energy dependent impact ionization rates for electrons [$\gamma_e(\epsilon)$] and holes [$\gamma_h(\epsilon)$] with a previously reported Monte Carlo model (37). We then simulate the temporal dependence of the total charge density (N) as follows:

$$N_e(t) = \int_0^\infty p_e(\epsilon) + (1 - e^{-\gamma_e(\epsilon)t})p_e(\epsilon)d\epsilon, \quad (5)$$

$$N_h(t) = \int_{-\infty}^0 p_h(\epsilon) + (1 - e^{-\gamma_h(\epsilon)t})p_h(\epsilon)d\epsilon, \quad (6)$$

$$N(t) = N_e(t) + N_h(t). \quad (7)$$

To phenomenologically account for the trapping of charge carriers we assume that the charge density (N) exponentially decreases with a characteristic time constant τ :

$$N(t) = N(t)e^{-t/\tau}. \quad (8)$$

Finally, we estimate the temporal dependence of the plasma frequency on the charge density as

$$\omega_{pl}(t) \approx \sqrt{N(t)}. \quad (9)$$

References

1. Z. Chen *et al.*, Ultrafast electron dynamics reveal the high potential of InSe for hot-carrier optoelectronics. *Physical Review B* **97**, 241201 (2018).
2. J. Sjakste *et al.*, Ultrafast dynamics of hot carriers: Theoretical approaches based on real-time propagation of carrier distributions. *The Journal of Chemical Physics* **162**, (2025).
3. J. Lloyd-Hughes *et al.*, The 2021 ultrafast spectroscopic probes of condensed matter roadmap. *Journal of Physics: Condensed Matter* **33**, 353001 (2021).
4. M. Na, A. K. Mills, D. J. Jones, Advancing time- and angle-resolved photoemission spectroscopy: The role of ultrafast laser development. *Physics Reports* **1036**, 1-47 (2023).

5. H. Tanimura *et al.*, Formation of hot-electron ensembles quasiequilibrated in momentum space by ultrafast momentum scattering of highly excited hot electrons photoinjected into the Γ valley of GaAs. *Physical Review B* **93**, (2016).
6. J. Sjakste, K. Tanimura, G. Barbarino, L. Perfetti, N. Vast, Hot electron relaxation dynamics in semiconductors: assessing the strength of the electron-phonon coupling from the theoretical and experimental viewpoints. *J Phys-Condens Mat* **30**, (2018).
7. H. Tanimura, J. Kanasaki, K. Tanimura, J. Sjakste, N. Vast, Ultrafast relaxation dynamics of highly excited hot electrons in silicon. *Physical Review B* **100**, (2019).
8. L. Rota, P. Lugli, T. Elsaesser, J. Shah, Ultrafast Thermalization of Photoexcited Carriers in Polar Semiconductors. *Physical Review B* **47**, 4226-4237 (1993).
9. I. Klett, B. Rethfeld, Relaxation of a nonequilibrium phonon distribution induced by femtosecond laser irradiation. *Physical Review B* **98**, (2018).
10. C. J. Kaplan *et al.*, Femtosecond tracking of carrier relaxation in germanium with extreme ultraviolet transient reflectivity. *Physical Review B* **97**, (2018).
11. H. Tanimura, K. Tanimura, J. Kanasaki, Ultrafast relaxation of photoinjected nonthermal electrons in the F valley of GaAs studied by time- and angle-resolved photoemission spectroscopy. *Physical Review B* **104**, (2021).
12. K. Tanimura, H. Tanimura, J. Kanasaki, Ultrafast dynamics of photoinjected electrons at the nonthermal regime in the intra-T-valley relaxation in InP studied by time- and angle-resolved photoemission spectroscopy. *Physical Review B* **106**, (2022).
13. M. Zurch *et al.*, Direct and simultaneous observation of ultrafast electron and hole dynamics in germanium. *Nat Commun* **8**, (2017).
14. M. Zürch *et al.*, Ultrafast carrier thermalization and trapping in silicon-germanium alloy probed by extreme ultraviolet transient absorption spectroscopy. *Struct Dynam-Us* **4**, (2017).
15. M. Wörle, A. W. Holleitner, R. Kienberger, H. Iglev, Ultrafast hot-carrier relaxation in silicon monitored by phase-resolved transient absorption spectroscopy. *Physical Review B* **104**, (2021).
16. M. Neuhaus *et al.*, Transient field-resolved reflectometry at 50-100 THz. *Optica* **9**, 42-49 (2022).
17. G. Inzani *et al.*, Field-driven attosecond charge dynamics in germanium. *Nature Photonics* **17**, 1059 (2023).
18. S. Keiber *et al.*, Electro-optic sampling of near-infrared waveforms. *Nature Photonics* **10**, 159 (2016).
19. S. Sederberg *et al.*, Attosecond optoelectronic field measurement in solids. *Nat Commun* **11**, (2020).
20. D. Zimin *et al.*, Petahertz-scale nonlinear photoconductive sampling in air. *Optica* **8**, 586-590 (2021).
21. M. R. Bionta *et al.*, On-chip sampling of optical fields with attosecond resolution. *Nature Photonics* **15**, 456-460 (2021).
22. S. B. Park *et al.*, Direct sampling of a light wave in air. *Optica* **5**, 402-408 (2018).
23. D. A. Zimin, V. S. Yakovlev, N. Karpowicz, Ultra-broadband all-optical sampling of optical waveforms. *Sci Adv* **8**, (2022).
24. Y. Y. Liu, J. E. Beetar, J. Nesper, S. Gholam-Mirzaei, M. Chini, Single-shot measurement of few-cycle optical waveforms on a chip. *Nature Photonics* **16**, 109 (2022).
25. D. A. Zimin, A. Ashoka, F. Reiter, A. Rao. (2025).
26. D. A. Zimin *et al.*, Dynamic optical response of solids following 1-fs-scale photoinjection. *Nature* **618**, 276 (2023).
27. K. Sokolowski-Tinten, D. von der Linde, Generation of dense electron-hole plasmas in silicon. *Physical Review B* **61**, 2643-2650 (2000).

28. A. Andrade-Neto, Dielectric function for free electron gas: comparison between Drude and Lindhard models. *Revista Brasileira de Ensino de Física* **39**, e2304 (2017).
29. <https://elk.sourceforge.io/>. (The Elk Code, (2025)).
30. F. Tran, P. Blaha, Accurate Band Gaps of Semiconductors and Insulators with a Semilocal Exchange-Correlation Potential. *Physical Review Letters* **102**, (2009).
31. M. Qasim, M. S. Wismer, M. Agarwal, V. S. Yakovlev, Ensemble properties of charge carriers injected by an ultrashort laser pulse. *Physical Review B* **98**, 214304 (2018).
32. S. A. Sato, Y. Shinohara, T. Otake, K. Yabana, Dielectric response of laser-excited silicon at finite electron temperature. *Physical Review B* **90**, (2014).
33. E. Gaubas, J. Vanhellemont, Dependence of carrier lifetime in germanium on resistivity and carrier injection level. *Appl Phys Lett* **89**, (2006).
34. V. G. Tyuterev, S. V. Obukhov, N. Vast, J. Sjakste, calculation of electron-phonon scattering time in germanium. *Physical Review B* **84**, (2011).
35. G. Mak, H. M. Vanderschuer, Femtosecond Transmission Spectroscopy at the Direct Band-Edge of Germanium. *Physical Review B* **49**, 16817-16820 (1994).
36. E. Cartier, M. V. Fischetti, E. A. Eklund, F. R. Mcfeely, Impact Ionization in Silicon. *Appl Phys Lett* **62**, 3339-3341 (1993).
37. B. Ghosh, X. Wang, X. F. Fan, L. F. Register, S. K. Banerjee, Monte Carlo study of germanium n- and pMOSFETs. *Ieee T Electron Dev* **52**, 547-553 (2005).
38. T. Sjödin, H. Petek, H. L. Dai, Ultrafast carrier dynamics in silicon: A two-color transient reflection grating study on a (111) surface. *Physical Review Letters* **81**, 5664-5667 (1998).
39. R. Kienberger *et al.*, Atomic transient recorder. *Nature* **427**, 817-821 (2004).
40. M. Qasim, D. A. Zimin, V. S. Yakovlev, Optical Gain in Solids after Ultrafast Strong-Field Excitation. *Physical Review Letters* **127**, (2021).
41. P. Giannozzi *et al.*, Advanced capabilities for materials modelling with Quantum ESPRESSO. *Journal of Physics: Condensed Matter* **29**, 465901 (2017).
42. G. Pizzi *et al.*, Wannier90 as a community code: new features and applications. *Journal of Physics: Condensed Matter* **32**, 165902 (2020).
43. S. Poncé, E. R. Margine, C. Verdi, F. Giustino, EPW: Electron–phonon coupling, transport and superconducting properties using maximally localized Wannier functions. *Computer Physics Communications* **209**, 116-133 (2016).

Acknowledgments

Computer time has been granted by the national centers GENCI-CINES and GENCI-TGCC (Project 2210), and by École Polytechnique through the 3Lab computing cluster.

Funding:

Swiss National Science Foundation (SPF grant no. TMPFP2 217068, D.A.Z.).

ANR DragHunt project ANR-24-CE50-3505 (J.S and R.S).

Authors contributions:

Conceptualization: D.A.Z., V.S.Y.

Methodology: D.A.Z.

Investigation: D.A.Z.

Theory: V.S.Y., J.S., D.A.Z., R.S., M.Q.

Visualization: D.A.Z., V.S.Y.

Supervision: D.A.Z., V.S.Y.

Writing—original draft: D.A.Z.

Writing—review & editing: V.S.Y., D.A.Z., J.S.

Competing interests: Authors declare that they have no competing interests.

Data and materials availability:

The datasets generated during and/or analyzed during the current study are available from the corresponding author upon reasonable request.

Figures and Tables

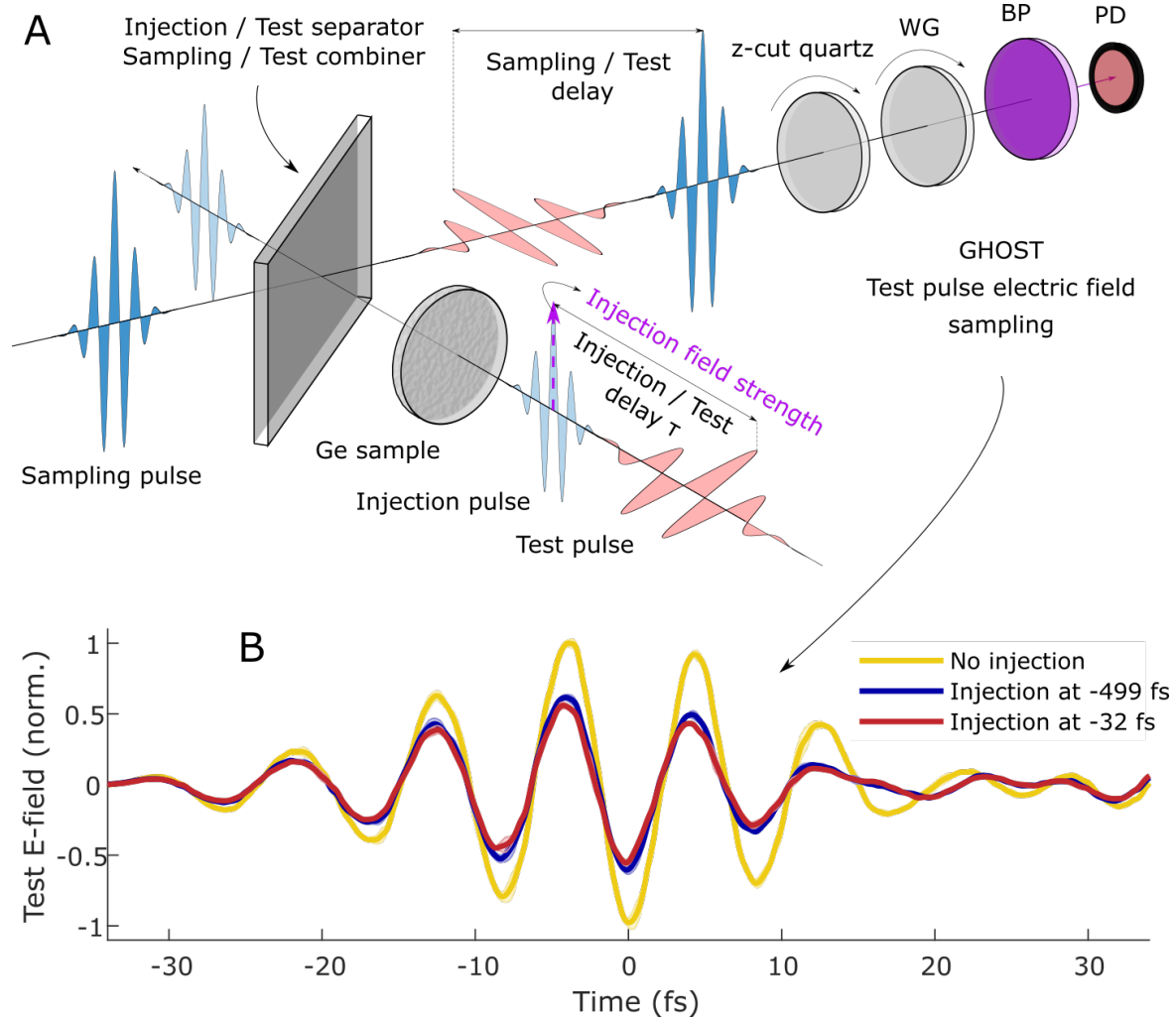


Fig. 1. Experimental concept and results. (A) Schematic of the experiment. Two orthogonally polarized pulses (test pulse and injection pulse) are incident on a polycrystalline germanium sample. After the interaction with the sample, the injection pulse is optically filtered out and the transmitted electric field of the test pulse is measured. The field-resolved measurement is repeated for various peak intensities of the injection pulse and various pump-probe delays, τ . (B) The measured waveform of the test pulse transmitted through the unperturbed sample (labeled "No injection") is compared to measurements where the sample is photoexcited by a 0.12-V/Å injection pulse at two different pump-probe delays: the maximum delay in our scan ($\tau = 499$ fs) and the delay where photoexcitation occurs at the beginning of the test pulse ($\tau = 32$ fs). Here WG is a wire-grid polarizer, BP is a bandpass filter while PD is a photodiode.

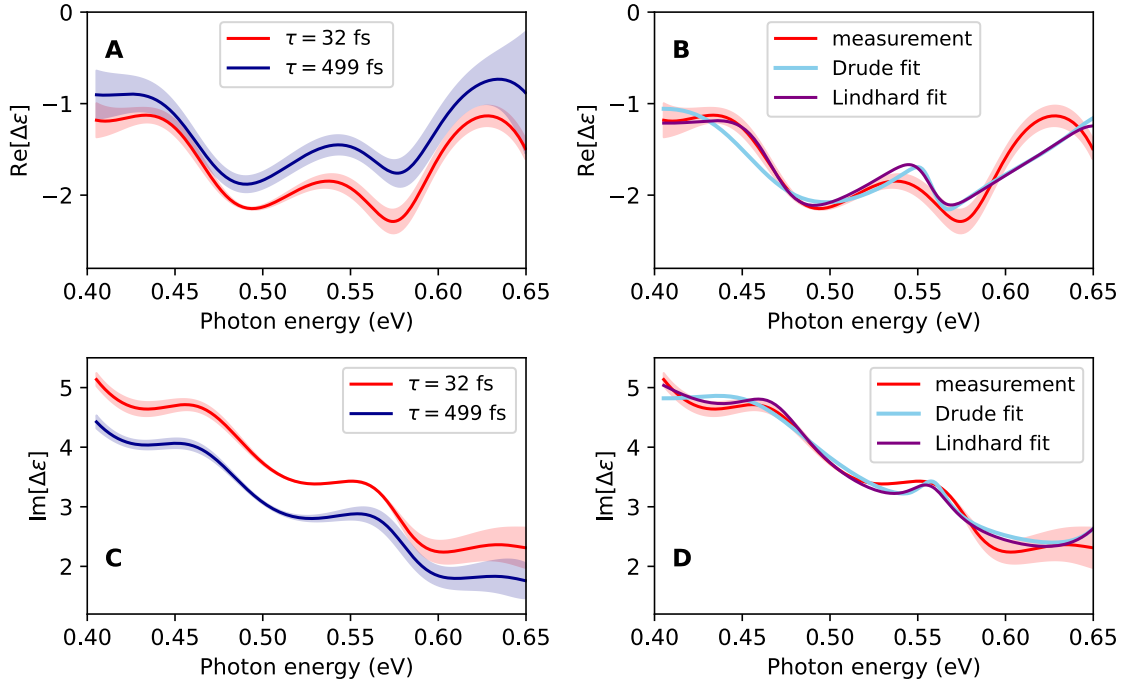


Fig. 2. Photoinjection-induced changes in the linear permittivity of germanium. The 0.12-V/Å injection pulse changes the linear real (A, B) and imaginary (C, D) parts of $\Delta\epsilon$. The solid lines in (A) and (C) represent the permittivity change evaluated from the waveforms in Fig. 1B, while the shaded areas indicate one standard deviation calculated from three consecutive measurements. Panels (B) and (D) compare the measurements at $\tau = 32$ fs with the Drude-Lorentz and Lindhard-Lorentz fitting models.

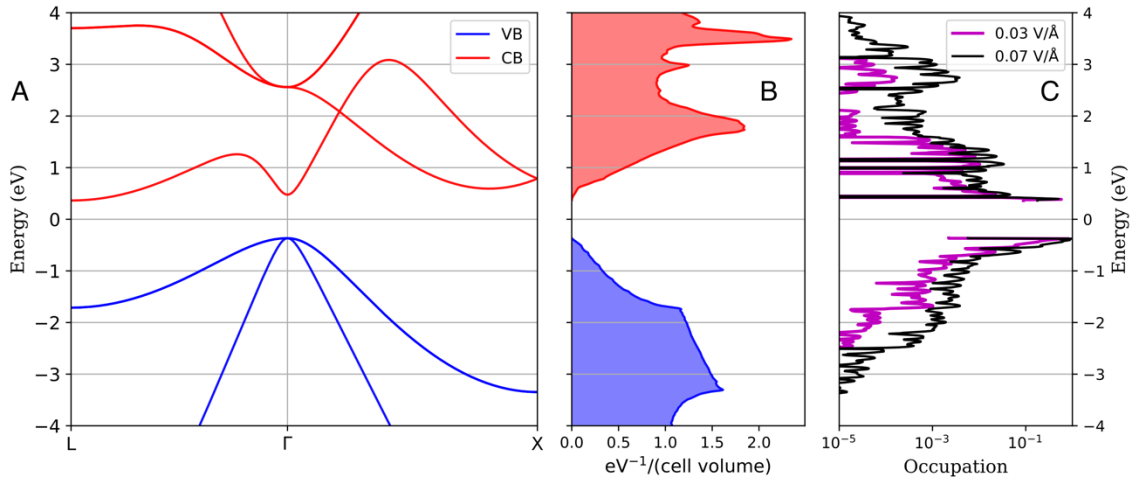


Fig. 3. Photoexcitation of germanium by the pump pulse. (A) Band structure, (B) density of states, and (C) energy-resolved carrier occupations obtained from density functional theory. Each data point in panel (C) represents the occupation probability averaged over all Bloch states at a given energy. The calculations were performed for peak injection fields of 0.03 V/Å and 0.07 V/Å within the medium (after transmission through the sample surface).

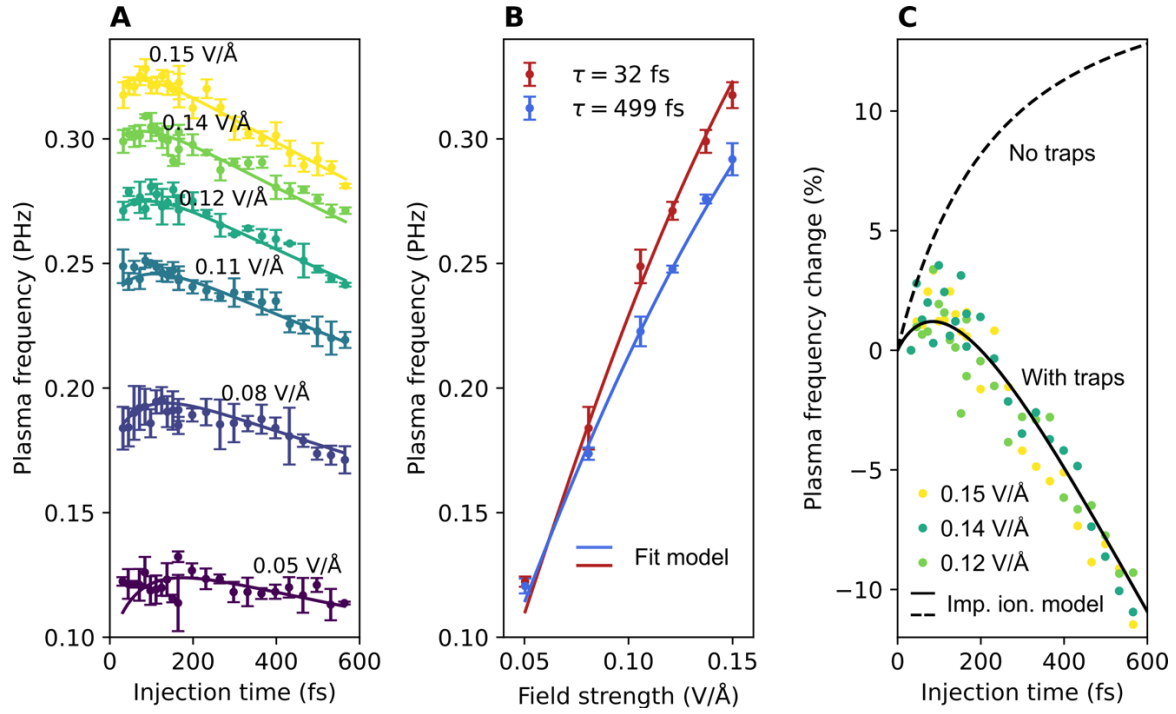


Fig. 4. Plasma frequency dynamics. (A) Time evolution of the plasma frequency for different injection field strengths. Solid lines show fits using the model of Eq. (3). (B) Plasma frequency versus injection field strength at early ($\tau = 32$ fs) and late ($\tau = 499$ fs) times of photoinjection. Solid lines are obtained from the fit model of Eq. (3) utilized for panel (A). (C) Comparison of the experiment (dots) and theoretical estimation based on the impact ionization model. The dashed black curve represents the plasma frequency dynamic obtained from the ab initio calculated electron and hole populations and incorporating Monte Carlo-derived impact ionization rates for germanium (37). The solid black curve shows the effect of charge trapping applied to the dashed black curve.